

## Hydrothermal Synthesis and Characterization of Sodium Bismuth Titanate for Photocatalytic Applications

Mohammed Mesrar<sup>1\*</sup>, Abdelhalim Elbasset<sup>1</sup>, Imane El Mrabet<sup>2</sup>, Hicham Zaitan<sup>3</sup>, Farid Abdi<sup>1</sup>, Nor-Said Echatoui<sup>1</sup>, Taj-dine Lamcharfi<sup>1</sup>

<sup>1</sup> Signals, Systems and Components Laboratory (LSSC), Faculty of Sciences and Technologies of Fez, Sidi Mohamed Ben Abdellah University, B.P. 2022, Imouzzar Road, Fez, Morocco

<sup>2</sup> Department of Physics-Chemistry, Polydisciplinary Faculty of Ouarzazate, University of Ibn Zohr, Ouarzazate, Morocco

<sup>3</sup> Laboratory of Processes, Materials and Environment (LPME), Faculty of Sciences and Technologies of Fez, Sidi Mohamed Ben Abdellah University, B.P. 2022, Imouzzar Road, Fez, Morocco

\* Corresponding author's e-mail: mohammed.mesrar@usmba.ac.ma

### ABSTRACT

Sodium bismuth titanate ( $\text{Na}_{0.5}\text{Bi}_{0.5}\text{TiO}_3$ , abbreviated NBT) ceramics underwent concurrent successful synthesis on the basis of the hydrothermal method. A selected low-temperature process of thermal treatment was conducted to obtain a highly dense morphology, produced from high purity carbonates and oxides serving as initial precursors. The presence of well-crystallized NBT in the rhombohedral phase was also found at hydrothermal temperatures of 200 °C. X-ray diffraction (DRX), Raman spectroscopy, Infrared spectroscopy (IR), and Scanning electron microscopy (SEM) analysis enabled to verify the structure, phase, morphology, and composition of the used samples. NBT ceramics exhibit features specific to relaxor ferroelectrics, with a diffusion exponent  $\gamma$  of up to 1.5 to promote their applications in micro-electromechanical and energy harvesting systems. The photocatalytic behaviors of NBT powders have been assessed by means of the degradation of methylene blue (MB) through UV-light irradiation. The samples prepared with precursors having a Na/Bi ratio of 0.5/0.5 showed the highest methylene blue (MB) photodegradation rate of 100% under UV irradiation for 420 minutes. In addition, photocatalytic activities under different masses and pH values were discussed for the first time. In addition, the photocatalyst has excellent stability, due to the larger particle size and surface area, which opens up new possibilities for the design of multi-component photocatalysts for future applications. The photocatalytic mechanism for the degradation of organic dyes (MB) has been principally assigned to the photoreduction process caused by superoxide radical anions ( $\text{O}^{2-}$ ) and hydroxyl radicals ( $\text{OH}$ ).

**Keywords:** hydrothermal method, methylene blue,  $\text{Na}_{0.5}\text{Bi}_{0.5}\text{TiO}_3$ , photocatalyst, raman spectroscopy.

### INTRODUCTION

The global trend of a growing global population (9 billion people by 2050), combined with increased urbanisation, industrialisation, and agriculture, means that the global demand for water is becoming increasingly pressing (Blum 2013; Fouilleux, Bricas, and Alpha 2017; Bhattacharyya, Das, and Omar 2019). However, domestic, industrial and agricultural discharges are leading to increased levels of air and water pollution as well as the emergence of new forms of pollution,

such as radioactive pollution, which are toxic to humans and ecosystems (González-Pleiter et al. 2013; Bhattacharyya et al. 2021). In accordance with European regulations (Water Framework Directive and Directive 2008/50/EC), wastewater treatment and purification systems fail to provide effective and cost-effective treatment solutions that meet the needs of sustainable development. These systems are based, for example in the case of water purification, on physical (filtration, adsorption on activated carbon), chemical or microbiological (use of bacteria) methods which must

sometimes be combined to obtain an acceptable degree of purification (Shannon et al. 2008). This requires time and several processing steps, which also involves additional costs. Furthermore, heterogeneous photocatalysis is one of the main modern technologies used in water purification, (Di Paola et al. 2012), the degradation of colorants (Huo et al. 2013) and the production of hydrogen (Fan et al. 2021). Indeed, it is a promising technique for the degradation of various pollutants. Economically, it is the most appropriate way of protecting the environment from the problems caused by industrial development. It permits the total degradation, by mineralisation at room temperature, of pollutants into CO<sub>2</sub> and H<sub>2</sub>O without any thermal energy input (Herrmann 1999). Furthermore, hydrothermal synthesis has a number of advantages over both conventional and non - conventional ceramic synthesis processes (Mohammed Mesrar, Elbasset, and Abdi 2023), together with energy efficiency, cost savings, clarity, higher dispersion, better nucleation, better shape control, higher rate of reaction, and lower functioning temperature (Trelcat et al. 2011; M. Mesrar 2022). Currently, several photocatalysts were tested for their photocatalytic efficiency towards harmful pollutants in water and air. Newly, a Na/Bi based-oxide photocatalysts have caught the much attention among researchers due to their band gap of less than 3eV. As examples, Bi<sub>2</sub>O<sub>3</sub> (Ammuri et al. 2014), BiFeO<sub>3</sub> (Lahmar et al. 2011) and Bi<sub>12</sub>Ti<sub>20</sub> (He et al. 2014; M. Mesrar et al. 2023), active in the UV and visible range, can be mentioned. Concerns have been raised about increasing energy conversion effectiveness, or about dye degradation that is generally linked to the generation, the bandgap of semiconductor powders, transfer of photoexcited electrons as well as holes, separation and the redox reaction that takes place at the surface within a photocatalyst. NBT seems very promising as a photocatalyst due to their interesting opto-electric and nonlinear optical properties, yet their yield is insufficient on account of the material's large band gap (~3.1eV) (Zhengwen Yang et al. 2009; Chen et al. 2017; M. Mesrar et al. 2022a). The objectives of the present work were: (1) to examine the effect of temperature on the formation mechanism of NBT, using a new approach based on oxides (Bi<sub>2</sub>O<sub>3</sub>, TiO<sub>2</sub>) and carbonates (Na<sub>2</sub>CO<sub>3</sub>) as a reactive source, on the structural, microstructural and dielectric properties of NBT ceramics processed by hydrothermal reaction. (2) Photocatalytic properties of the synthesized NBT

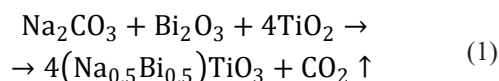
nanostructures were evaluated by decomposing (MB) under visible light irradiation. The obtained results show that the photocatalytic degradation efficiency of methylene blue (MB) reaches 100% after 420 minutes of irradiation. The functional mechanism of photocatalysis has been carefully investigated and correlated.

## EXPERIMENTAL

### Sample preparation

All ceramics from the hydrothermal technique have been acquired by blending carbonate (Na<sub>2</sub>CO<sub>3</sub>) of high purity and oxide (Bi<sub>2</sub>O<sub>3</sub> and TiO<sub>2</sub>) (Sigma-Aldrich 99.96%). Sodium hydroxide (NaOH) was utilized to act as a source of sodium cations while still maintaining a strongly basic environment. The pH was subsequently regulated to 10 by adding drops of 10M (NaOH) aqueous solution at a time. Stoichiometric quantities of the precursors were weighed and mixed with acetone according to the general chemical equation. The resulting mixture was then dried and deagglomerated by means of an agate mortar to achieve the appropriate NBT composition. The powder was subsequently placed in a Teflon autoclave inside a steel vessel (50 ml capacity) and heated to 200 °C for 24 hours. Finally, the powder was gathered, centrifuged, and washed several times effectively over with distilled water until the pH of the starting solution attained pH~7, after which it was dried at 80 °C for 12 hours. Figure 1 presents briefly the different steps adopted for the elaboration of the studied ceramics. Temperature is very important in the synthesis. It directly influences the solubility of the different precursors used as well as the kinetics of the chemical reaction.

The chemical reaction of this synthesis is represented by the following equation:



In order to know precisely the temperature of the hydrothermal reaction for the establishment the pure phase of NBT, different temperatures were tested (140 °C, 160 °C, 180 °C and 200 °C) for a duration of 24 h, respectively in a strongly basic medium (pH=10). A compromise between sodium hydroxide concentration (pH=10) and synthesis temperature seems inevitable. Indeed, for a time of 24 hours, only a high concentration

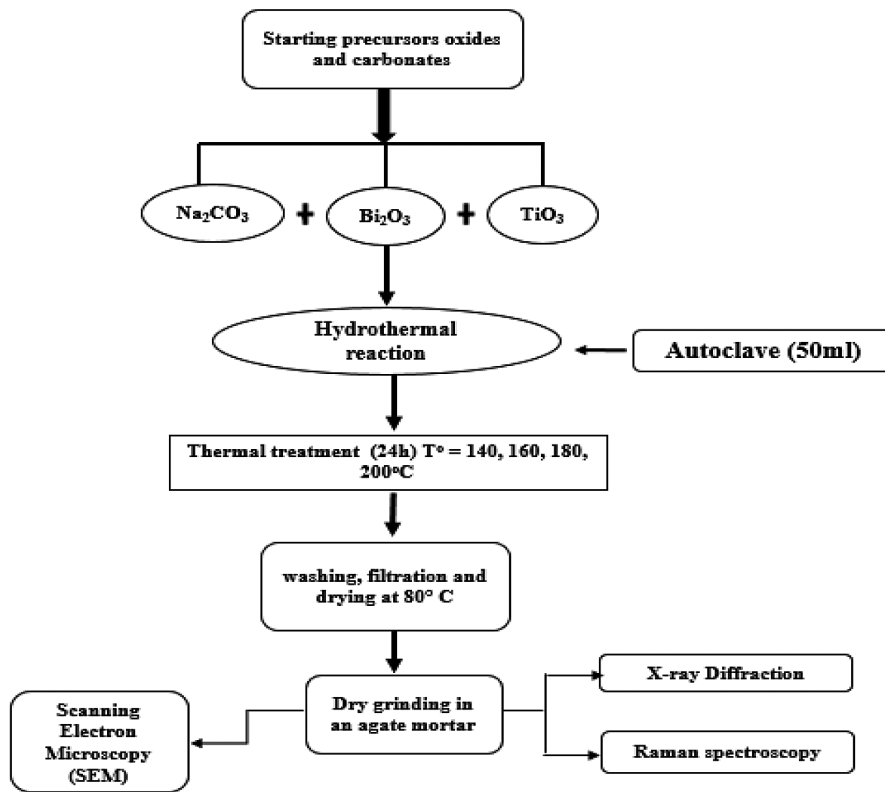


Figure 1. Graphical depiction of all the steps in the synthesis of NBT samples

of sodium hydroxide (pH=10) yields a nicely defined X-ray diffractogram to be obtained. The powder formed was deagglomerated by means of an agate mortar in the presence of a few drops of polyvinyl alcohol (3% PVA) (binder and plasticiser). The powders of the studied sample have been pressed by means of uniaxial force so as to yield pellets having a diameter of 12 mm and a thickness of about 1 mm, under a pressure of 8 tons/cm<sup>2</sup> for 5 min, then these pellets have been sintered for 4 hours at a temperature of 1000 °C.

### Characterization of NBT

The ceramic samples were phase determined using X-ray diffraction analysis (XRD) based on an X-ray diffractometer device (XPRT-PRO) equipped with a CuK radiation source. The Rietveld fitting of the diffraction data yielded weight fractions, crystallite sizes, crystalline fractions, and lattice constants. The grain morphology and microstructure of the studied samples have been examined by means of a scanning electron microscope (SEM). Raman spectroscopy has been successfully employed as an excellent technique to investigate the structural evolution of ceramics; measurements were carried out by the Labram

O10 (Jobin-Yvon) with one He-Ne (633 nm) laser source with a nominal power of 15 mW. The dielectric properties as a function of temperature were studied by means of a LCR-Meter (Agilent 4284A) analyser for a wide range of frequencies up to 1MHz with a temperature increase of about 3 °C min<sup>-1</sup>.

### Set-up of the photocatalytic experiment for MB degradation

To better assess the photocatalytic activity of the studied hydrothermally produced NBT-material for the degradation of MB, experimental tests have been performed in a photoreactor endowed with three UV-A lamps described in detail in previous work (El Mrabet et al. 2018). Hence, a stock solution of MB of mass concentration 10 mg/L was prepared. The mass of NBT was varied by 0.25, 0.5, and 1 mg/L to determine the optimal catalyst amount at which the photocatalytic efficiency should be highest. The effect of MB solution pH (3.5, 8, and 12) on MB photodegradation efficiency was also investigated. Noting that the initial pH of MB solution without any adjustment is 8, then it was adjusted to pH=3.5 and pH=12 using H<sub>2</sub>SO<sub>4</sub> (2M) and NaOH (2M),

respectively. For each test, the catalyst mass and MB solution were introduced in a pyrex reactor and stirred for 60 min under dark conditions to reach the adsorption equilibrium, then, the three lamps were turned on to start the photocatalysis reaction. Consequently, the removal efficiency was assessed every 60 minutes by sampling a volume of 4 mL that was centrifuged at 4000 rpm for 10 minutes and analysed using the spectrophotometry method at 663 nm. The MB degradation efficiency has been determined by means of UV-visible absorption measurements were carried out on the basis of the spectrophotometer. The photodegradation removal efficiency was also performed based on the following equation:

$$\text{MB Removal \%} = \frac{(C_i - C_f)}{C_i} * 100 \quad (2)$$

where:  $C_i$  and  $C_f$  are the BM concentrations at  $t = 0$  and  $t \neq 0$  of the contact time, respectively.

## RESULTS AND DISCUSSION

### X-ray diffraction (XRD) analysis

Figure 2 displays the XRD plots of the different powders hydrothermally treated at various temperatures 140, 160, 180 and 200 °C for a duration of 24 hours with NaOH concentration of 10 M. In addition, characteristic peaks that are consistent with NBT (JCPDS No. 36-0340) (Pookmanee et al. 2004; Mohammed Mesrar et al. 2022) have started to develop at a temperature of 140 °C,

although the intensity of the peak remains low. Thus, the impurity phase  $\text{Bi}_4\text{Ti}_3\text{O}_{12}$  (marked as black round circle) was detected as well as a Bi rich phase. This suggests that the crystallinity of this sample was very low. In the conducted experiment, the Bi-rich phase, as well as the pyrochlore phase  $\text{Bi}_4\text{Ti}_3\text{O}_{12}$  (BTO), are thermodynamically stable up to 160 °C, according to Lencka (Lencka, Oledzka, and Riman 2000). A pure NBT phase could be produced in the temperature interval of 120-200 °C, as demonstrated by Sui et al (Sui et al. 2013). Furthermore, increasing the synthesis time aided in the stabilization of the required phase; however, increasing the synthesis temperature to 200 °C resulted in an additional reflection in the X-ray diffraction pattern of the obtained reaction product that has been assigned to the perovskite phase in  $\text{Bi}_4\text{Ti}_3\text{O}_{12}$  (BTO). With increasing temperature (above 160 °C), the height of the diffraction peaks of the studied samples increased whereas the total width at half maximum decreased.

Through increasing the temperature to 200 °C, the diffraction diagram displays distinct diffraction peaks, indicating a successful crystallization. The findings suggest that an appropriate concentration of NaOH (10M) promotes the crystallization of NBT. This could be attributed to the fact that the NaOH served as a the A-site metal supplier to the perovskite lattice and also as a pH adjuster during the NBT formation reactions (X. P. Jiang et al. 2010). Structural refinement of the NBT ceramic was conducted using the Rietveld refinement technique, as demonstrated in Figure 3

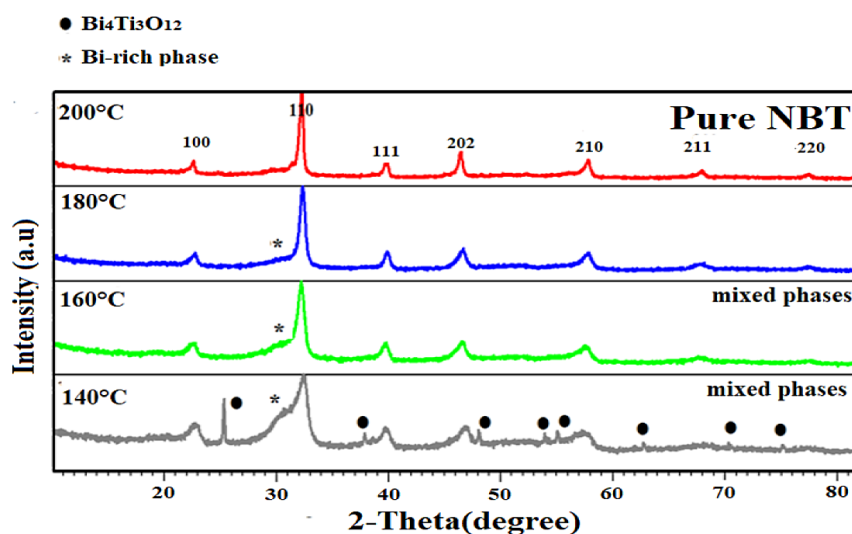


**Figure 2.** X-ray diffraction diagram of NBT powder produced using the hydrothermal method, treated at different temperatures (140, 160, 180 and 200 °C)

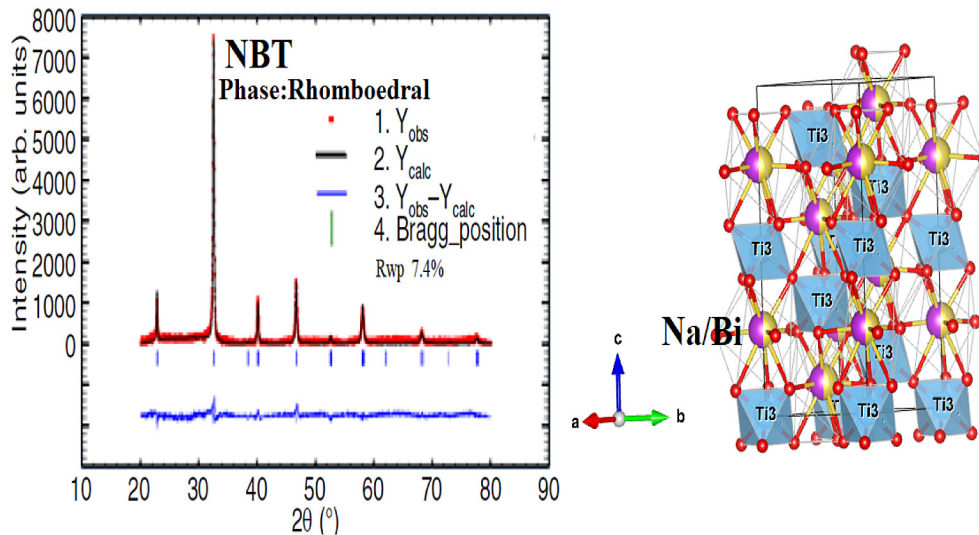


**Figure 3.** Rietveld refinement for compounds NBT treated at 200 °C

(Rietveld 1967; M. Mesrar et al. 2022a). The NBT fitted profiles were determined using the FullProf software. The peak profiles were defined using the pseudo-Voigt function. It is worth noting that the various symmetry groups have been carefully investigated. The experimentally observed and theoretically calculated XRD pattern profiles exhibit a small difference, as indicated by a blue line ( $Y_{\text{Observed}} - Y_{\text{Calculated}}$ ). The adjustment parameter ( $\chi^2$ ) indicates a satisfactory refinement result. Upon continued refinement, the  $\chi^2$  values of the sample are less than 1.65. The unit cell parameters of the crude NBT substrate are  $a = b = 5.4871 \text{ \AA}$ ,  $c = 13.4721 \text{ \AA}$  and  $\alpha = \beta = 90^\circ$ ,  $\gamma = 120^\circ$ , which is similar to previously reported data (M. Mesrar et al. 2019; Moon et al. 2011; Bhattacharyya and Omar 2018).

It should be noted that the reflections from this phase lack the characteristic splitting of a rhombohedral distortion of the perovskite cells, which can be explained by the fact that the synthesised product is consists of nanoparticles with a mean size of 161 nm, as determined by the Debye-Scherrer formula (Baerlocher and McCusker 1994; M. Mesrar et al. 2023; M. Mesrar et al. 2018). The cell parameters are grouped in Table.1.

### Raman scattering powder analysis

A vibrational study by Raman spectroscopy of the crystal lattice atoms of pure perovskite NBT is carried out to determine the active vibrational modes (Fig.4).  $(\text{Na}_{0.5}\text{Bi}_{0.5})\text{TiO}_3$  has four distinct bands of the rhombohedral phase of R3c space group. Furthermore, the obtained spectrum is consistent with that obtained in previous work (Jan Suchanicz, Jankowska-Sumara, and Kruzina 2011; M. Mesrar 2022; Mohammed Mesrar, Elbasset, and Abdi 2023). The irreducible representations of the optical modes of NBT are obtained using group theory:

$$\Gamma_{\text{vib}} = 4A_1 \oplus 9E \quad (3)$$

The modes  $A_1$  and  $E$  are polarized phonons, which means they are active in both Raman and IR at the same time. The tight lines of the two longitudinal and transversal phonon modes  $A_1$  (TO),  $A_1$ (LO) are observed at  $136 \text{ cm}^{-1}$  and  $280 \text{ cm}^{-1}$ , respectively. This corresponds to the obtained findings. The Raman bands of the studied NBT product are rather wide, as is typical for base relaxors-perovskite ferroelectrics. The expansion is mainly caused by a cationic problem at the 12-fold coordinated site (Quittet et al.

**Table 1.** Structural parameters Refined of NBT prepared by using the hydrothermal method

Lattice parameters	Space group	Cryst. Size (nm)	Density (g/cm <sup>3</sup> )	Reliability parameters $\chi^2$	NBT						
					Atom	Site	x	y	z	B(Å)	Occupancy
a(Å) = 5.487	R3c	161	5.95	1.65	Na <sup>+</sup> /Bi <sup>3+</sup>	6a	0	0	0.252	0.79	0.5/0.5
b(Å) = 5.487	-	-	-	-	Ti	6a	0	0	0.007	0.47	1
c(Å) = 13.472	-	-	-	-	O	18b	0.127	0.251	0.071	1.91	1
V(Å <sup>3</sup> ) = 365.12	-	-	-	-							

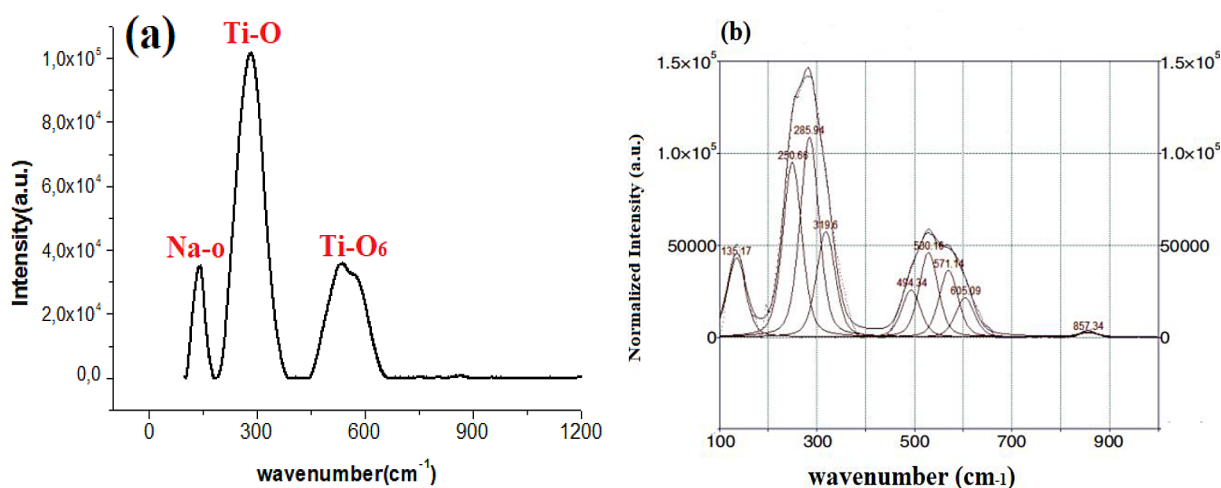


Figure 4. (a) Raman spectra of NBT ceramics and (b) the deconvoluted Raman spectra

1976). Kreisel et al (Kreisel et al. 2001) assigned the following modes of vibration to materials containing an oxygenated octahedral: an external mode of vibration for external octahedral liaisons represented by bands at low frequencies, and an internal mode of vibration for all internal octahedral vibrations appearing at high frequencies. Indeed, the low-frequency bands correspond to the vibration of the Na-O bond, which is situated near 136 cm<sup>-1</sup>. The 280 cm<sup>-1</sup> modes and the bands lie at higher frequencies (530 and 830 cm<sup>-1</sup>) that are associated with the vibration of the Ti-O bond in the TiO<sub>6</sub> octahedral (M. Mesrar et al. 2022b). Owing to the high mass of the bismuth atom, however, a Bi-O bond would be located at extremely low frequencies and it was not actually identified here.

### Microstructural study

Analysis via scanning electron microscopy (SEM) of the sample is illustrated in Figure 5. The NBT sample is composed of hexagonal shaped grains with a mean size of about 6.54 μm. The grain size is about 6.54 μm. The sample has a low porosity, which shows a high degree of cohesion and homogeneity between the grains. In the hydrothermal process, the alkaline medium, as a variable, is strongly related to the particle size, which leads to an improvement in particle size. As a result, it can be seen in this study that with a relatively high concentration of NaOH (10M), the rate of grain growth increases, and thus large particles of similar size are formed, depending on the hydrothermal temperature chosen. This finding is in good agreement with that of Zeroual et al (Zeroual et al. 2019; Sidi et al. 2019), obtained for NBT synthesized by the hydrothermal route at 24 hrs.

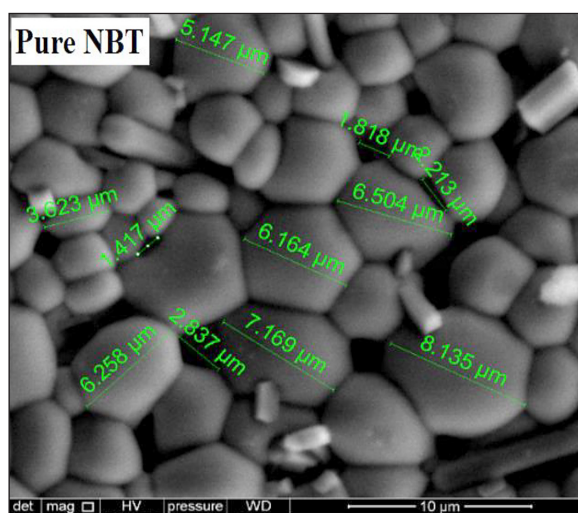
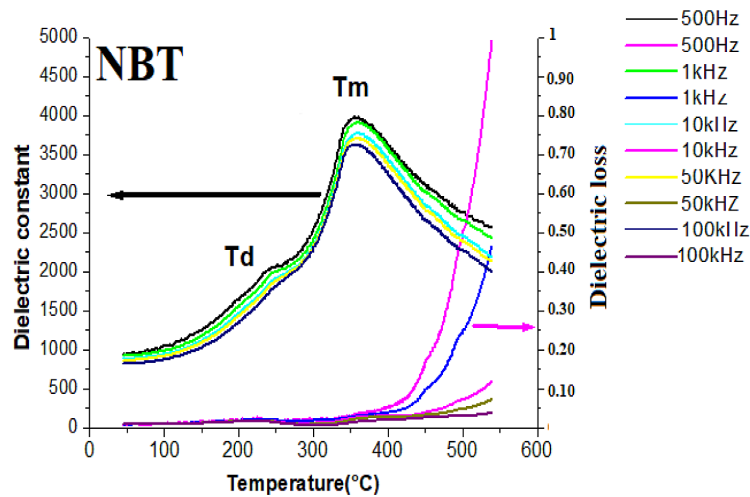


Figure 5. Scanning electron microscope (SEM) picture of the NBT sample sintered at 1000 °C for 4 hours

### Dielectric measurements

Figure 6 shows the thermal evolution of the relative permittivity ( $\epsilon_r$ ) and dielectric losses ( $\tan\delta$ ) of the NBT composition at different frequencies. The curves obtained reveal two dielectric anomalies: A shoulder anomaly, observed around 220 °C and slightly dependent on frequency (see the  $T_d$  region) (Mohammed Mesrar et al. 2019). The second anomaly reflected by an extended maximum in permittivity is observed at around 320 °C (see the  $T_m$  region) (Hiruma, Nagata, and Takenaka 2006). Thus, the temperature associated with the maximum in the relative permittivity ( $\epsilon_r$ ) is called the maximum temperature ( $T_m$ ) and corresponds to the anti-ferroelectric-paraelectric transition (Eric Cross 1987). Furthermore, the ferroelectric-paraelectric phase transition temperature changes with increasing frequency and shows a diffuse behaviour



**Figure 6.** Dielectric constant values of NBT sample processed hydrothermally and sintered at 1000 °C during 4hours as a function of temperature at different frequencies

(J. Suchanicz and Kwapuliski 1995). At low temperatures ( $T < 300$  °C) and at a given frequency the dielectric losses are constant and almost negligible, then they increase rapidly along with temperature until they reach a maximum value. These findings are in good agreement with previously published results (Barick et al. 2011; Hiruma, Nagata, and Takenaka 2006; Swain, Kumar Kar, and Kumar 2015). The value of the dielectric constant ( $\epsilon_{r_{max}}$ ) at  $T_m$  is about 3800 at 1KHz so this value is higher than that found in the literature (Shih, Aguadero, and Skinner 2018). This improvement is probably influenced by the increase in the average grain size ( $\sim 6$   $\mu\text{m}$ ) observed in the studied samples (Neusel and Schneider 2014; Zetian Yang et al. 2019).

The permittivity curves obtained show a dispersion according to of frequency (2nd anomaly), at temperatures between 340-360 °C. This diffuse phase transition has also been observed by many authors, including Sundarakannan et al (Sundarakannan, Kakimoto, and Ohsato 2003) and Birol et al (Birol, Damjanovic, and Setter 2005) in complex perovskite ferroelectrics ( $\text{KN bO}_3$ ). This behaviour can be linked to the coexistence of complex cations ( $\text{Na}^+$  and  $\text{Bi}^{3+}$ ), which have very nearly the same radii but also have significantly varied charges and electrotechnical configurations in an equivalent crystallographic site A. The variation of the dielectric losses ( $\tan\delta$ ) with temperature is shown in the figure above. It can be seen that the losses are relatively small up to  $T_m$  and then increase sharply with temperature. This increase can be attributed to electrical conductivity (Roukos et al. 2019). These findings are in good accord with current literature (Li, Feng, and Yao 2004).

### Transition diffuseness

For clarifying the behaviour of the material and to highlight the diffuse character of the transition, a modification of Uchino's law has been proposed by N.S. Echatoui et al (Echatoui, news, and 2005, n.d.) to describe the diffuse transition by the following relation:

$$\frac{1}{\epsilon_r} = \frac{1}{\epsilon_{r_{max}}} \left[ 1 + \frac{(T - T_m)^\gamma}{2\delta^\gamma} \right] \quad (4)$$

The curve of  $(\epsilon_{r_{max}}/\epsilon_r)$  versus  $(T-T_m)^\gamma$  of the NBT sample at 5 kHz is shown in Figure 7. For the sample of NBT, a linear relationship is established. The value of  $\gamma$  is established from equation, using the Matlab software (Elhorst 2014). The star symbol in the figure above corresponds to

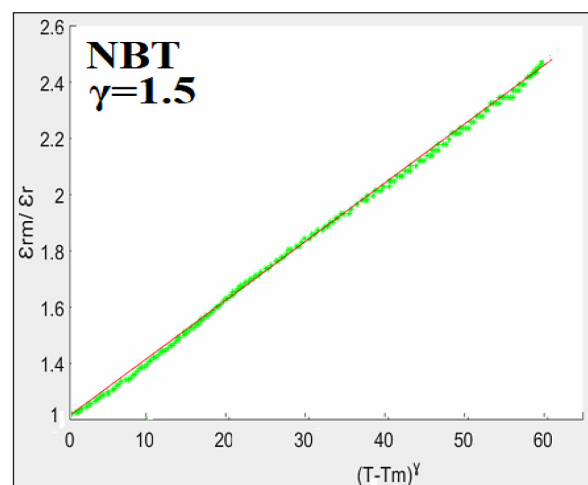


**Figure 7.** Fitting results of the dielectric permittivity ( $\epsilon_r$ ) data of the NBT sample to the modified Uchino law at 5 kHz

the experimental data, while the brown line represents the fit corresponding to the modified Uchino law. The value of  $\gamma$  is of the order of 1.5 and that of  $\delta$  is 95, this obviously means that this ceramic has a very diffuse character. This observed behaviour could be assigned to the cationic disorder at the A( $\text{Na}^+/\text{Bi}^{3+}$ ) site. Therefore, X-ray diffraction analysis allowed us to highlight this local disordering between the  $\text{Na}^+$  and  $\text{Bi}^{3+}$  cations.

### Adsorptive and photocatalytic activities of NBT

In order to investigate the removal efficiency of MB under UV-A irradiation (Photolysis), NBT alone (Adsorption), and NBT+UV-A (Photocatalysis), Fig. 8A presents the comparison of the MB removal using the three treatments. It is clearly shown that the photolysis has attained the lowest degradation efficiency that reached 1.44% after 420 min and 19% after 1920 min. While the adsorption process using NBT alone (without UV-A irradiations) removed 40% after 60 min that was fixed as  $t = 0$  for the photocatalysis treatment, then it raised slowly to achieve 48% at 1920 min.

On other hand, the MB degradation using photocatalysis treatment (NBT+UV-A) was significantly improved as a function of contact time where it achieved 66% after 300 min of UV-A illumination then the efficiency reached 99% at 1920 min which confirms the photocatalytic nature of the reaction. Moreover, Fig. 8B

illustrates the visible spectra of MB solution related to the initial concentration ( $t = 0$ ; 10 mg/L), to the solution sampled after 1440 min of photocatalysis test, and to the solution at the end of the treatment. A remarkable reduction of absorbance values is noticed according to the photodegradation time which corresponds to the visual discoloration of the samples (a) and (b) shown in the attached image. Therefore, due to the significant efficiency of the photocatalysis process (NBT+UV-A) compared to the adsorption and photolysis, the effect of NBT mass and the initial pH of MB solution under the UV-A illumination were further investigated. Moreover, the remarkable efficiency of methylene blue (MB) degradation in the presence of NBT particles and UV-A light might well be explained by the high oxidizing capacity of hydroxyl radicals ( $\cdot\text{OH}$ ) and superoxide radicals ( $\cdot\text{O}_2^-$ ) produced during the photocatalysis reactions. Indeed, it is well known that the photocatalytic activity of the semiconductors is related to the absorption of photons energy the irradiation corresponding to the bandgap of these semiconductors. In this study, once the NBT is irradiated with UV-A light, the free electron-hole ( $e^-h^+$ ) pairs are generated. The excited electrons in the conduction band ( $e^-_{\text{CB}}$ ) react with the dissolved oxygen ( $\text{O}_2$ ) to produce superoxide radicals ( $\cdot\text{O}_2^-$ ). Moreover, the hydroxyl radicals ( $\cdot\text{OH}$ ) are produced by the reaction of  $\text{O}_2^{\cdot-}$  with water or by the interaction of the holes with hydroxyl ions or with water. Therefore, the produced  $\text{O}_2^{\cdot-}$

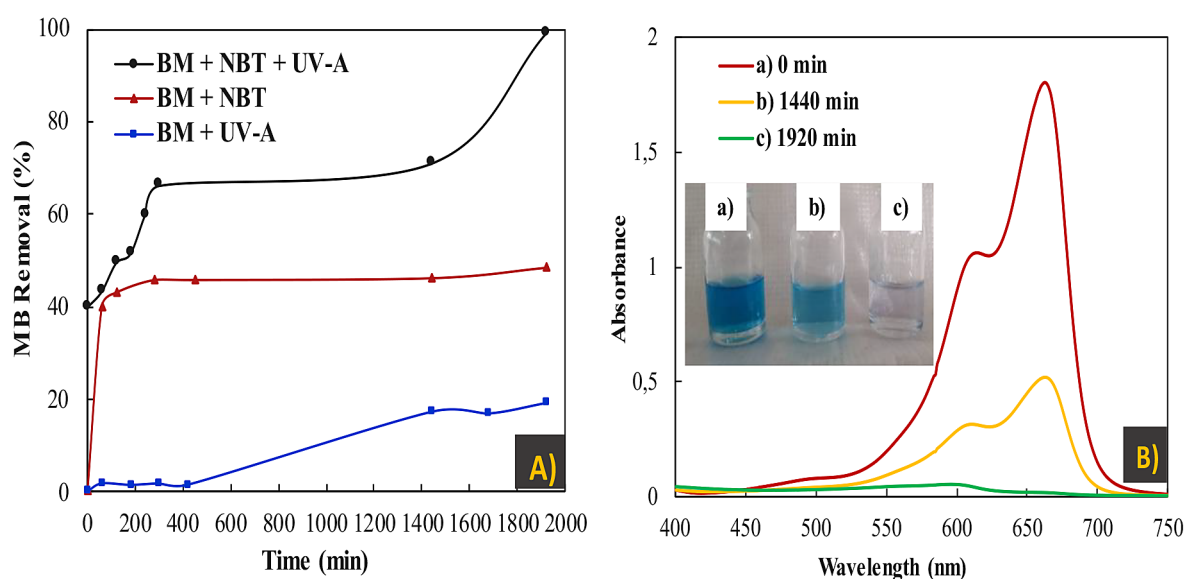


**Figure 8.** (A) Photodegradation kinetics of MB in the presence of UV, NBT, and NBT+UV ( $C_0(\text{BM})= 10 \text{ mg/L}$ ; NBT mass= 1g/L; initial pH=8) and (B) Visible spectra of MB solution before and after the photodegradation using NBT+UV-A

and  $\cdot\text{OH}$  as highly reactive and oxidizing species react with MB molecule and degrade it into simple and non-toxic products such as  $\text{H}_2\text{O}$  and  $\text{CO}_2$  (Goutham et al. 2021; Y. Jiang et al. 2021; Kurra et al. 2019).

### The effect of catalyst mass

To assess the influence of the NBT mass on the MB photodegradation, Fig. 9 presents the photodegradation efficiency of MB using 0.25, 0.50, and 1g/L of NBT during 1920 minutes of UV-A irradiation. The results indicate a notable effect of the catalyst mass on the MB removal under UV-A.

Indeed, the highest efficiency was observed using 1g/L 66% and 99% at 300 min and 1920 min, respectively, followed by 0.5g/L that removed 60% and 90%, while 0.25g/L resulted in the lowest photodegradation of 57% and 74% at the same mentioned moments of contact time.

### The effect of pH

The photocatalytic degradation process occurs as a result of both from the nature of the surface charges carried by the ferroelectric material NBT the ionic state of the pigment molecules, the adsorption of the dye, and the concentration of the hydroxyl radicals formed.

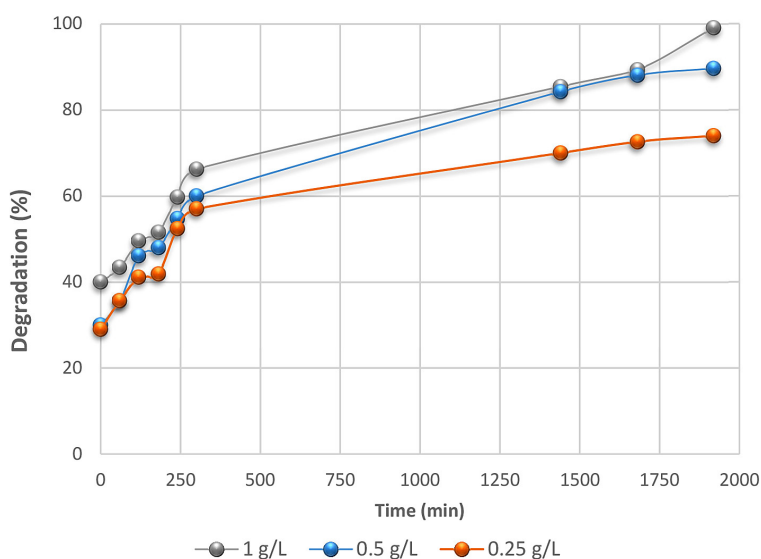


Figure 9. Degradation efficiency of MB using 0.25, 0.5 and 1 g/L of NBT ( $C_0(\text{BM}) = 10 \text{ mg/L}$ ; initial  $\text{pH} = 8$ )

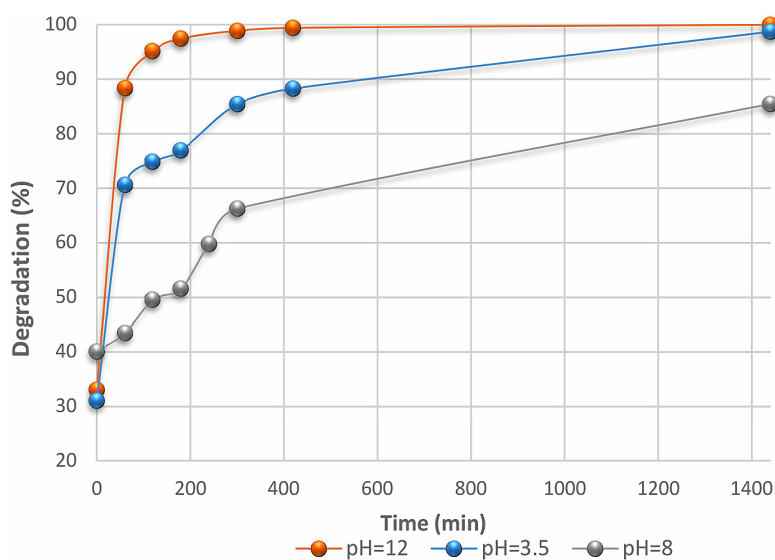


Figure 10. Degradation efficiency of MB as a function of pH (3.5; 8; and 12) under NBT mass = 1 g/L and  $C_0(\text{BM}) = 10 \text{ mg/L}$

All these properties depend on the pH because of its influence on the electrical charge of the photocatalyst surface. To investigate the influence of pH on the photodegradation of methylene blue in the presence of NBT under UV-A, three different pH values of MB solution were studied: 3.5, 8, and 12 using the catalyst mass of 1g/L. Figure 10 shows that the rate of decolourisation is higher with increasing pH values. Thus, the photocatalytic degradation of MB by the photocatalyst NBT is maximal for the pH value equal to 12. As a result, the basic nature of the environment favours the degradation of MB related to the phenomenon of adsorption of pollutants. Indeed, according to previous works that studied MB photodegradation (Tang, Zou, and Ye 2005; Azeez et al. 2018; Xiao et al. 2007) and similar cationic dye Blue Basic 41 (BB41) (Tanji et al. 2022), alkaline pH was found to be optimal. Those studies indicated that the degradation of MB and BB41 is enhanced at alkaline pH ( $\geq 11$ ). Tanji et al. and Xiao et al. reported that this result may be due to the fact that the hydroxyl ions  $\text{OH}^-$  adsorbed on the catalyst surface may promote the production of  $\text{OH}^\cdot$  which are the most oxidizing species (Tanji et al. 2022). Another explanation provided by Tang et al. and Azeez et al. is that the  $\text{OH}^-$  could favor the electrostatic attraction enhancing consequently the adsorption of MB which is the key step for the degradation of organic molecules by the photocatalysis process (Tang, Zou, and Ye 2005; Azeez et al. 2018). In this context, the pH effect has always been a challenging parameter in many studies where the results are often difficult to interpret and the point of zero charge of a catalyst is not always a crucial indicator to choosing the optimal pH (Tanji et al. 2019). The study of the photodegradation of MB by NBT oxide allows concluding that the best result (up to 100% during 420 min) is obtained using the catalyst mass of 1g/L and the pH value around 12.

## CONCLUSIONS

Hydrothermal synthesis enabled us to prepare NBT ceramics under the most optimal conditions at 200 °C for 24 hours and a 10M NaOH concentration. This process allowed reducing the calcination temperature compared to the solid (~1000 °C) and sol-gel (~800 °C) route. Hence, the hydrothermal process could be adopted as an effective method and a favourable protocol for

the successful synthesis of highly photoactive perovskite materials. Analysis of the X-ray diffraction (XRD) peaks revealed that the studied specimens crystallize in the structure of rhombohedral symmetry (R3c) and lattice parameters:  $a = 5.48\text{\AA}$  and  $c = 13.47\text{\AA}$ . The pH concentration was significant role in the particle size, impurity, crystalline degree and the band gaps of the NBT materials. The variation in  $\gamma$  values is caused by the increased diffusivity in the proximity of the phase transition, which confirms the enhanced relaxor nature of NBT ceramics synthesised by this route. The NBT sample sintered at 1000 °C presented the highest photocatalytic activity for MB degradation under UV light as a result of the restricted band gap, higher crystallinity and higher oxygen adsorption. The results showed also a substantial enhancement in photocatalytic efficiency in the presence of UV irradiation with increasing the photocatalyst mass (1g/L) and pH (12) of the medium so that a 100% removal rate during 420 minutes was achieved which offers promising perspectives for the wastewater treatment by the photocatalysis technique.

## REFERENCES

1. Ammuri, A, S Hejiouej, K Ziat, and M Saidi. 2014. Photodegradation of Methyl Orange in Solution in Presence of Bismuth Trioxide. *Environ. Sci* 5 (S1): 2066–72.
2. Azeez, Fadhel, Entesar Al-Hetlani, Mona Arafa, Yasser Abdelmonem, Ahmed Abdel Nazeer, Mohamed O. Amin, and Metwally Madkour. 2018. The Effect of Surface Charge on Photocatalytic Degradation of Methylene Blue Dye Using Chargeable Titania Nanoparticles. *Scientific Reports* 8 (1): 1–9. <https://doi.org/10.1038/s41598-018-25673-5>.
3. Baerlocher, Christian, and Lynne B. McCusker. 1994. Practical Aspects of Powder Diffraction Data Analysis. *Studies in Surface Science and Catalysis* 85 (C): 391–428. [https://doi.org/10.1016/S0167-2991\(08\)60775-2](https://doi.org/10.1016/S0167-2991(08)60775-2).
4. Barick, B. K., K. K. Mishra, A. K. Arora, R. N.P. Choudhary, and Dillip K. Pradhan. 2011. Impedance and Raman Spectroscopic Studies of  $(\text{Na}_{0.5}\text{Bi}_{0.5})\text{TiO}_3$ . *Journal of Physics D: Applied Physics* 44 (35). <https://doi.org/10.1088/0022-3727/44/35/355402>.
5. Bhattacharyya, Rahul, Soumitra Das, Amit Das, and Shobit Omar. 2021. Effect of Sintering Temperature on the Microstructure and Conductivity of  $\text{Na}_{0.54}\text{Bi}_{0.46}\text{Ti}_{0.99}\text{Mg}_{0.01}\text{O}_{3-\delta}$ . *Solid State Ionics* 360 (February): 115547. <https://doi.org/10.1016/J.SSI.2020.115547>.

6. Bhattacharyya, Rahul, Soumitra Das, and Shobit Omar. 2019. Long-Term Conductivity Stability of Acceptor-Doped  $\text{Na}_{0.54}\text{Bi}_{0.46}\text{TiO}_{3-\delta}$ . *Solid State Ionics* 330 (February): 40–46. <https://doi.org/10.1016/J.SSI.2018.12.009>.
7. Bhattacharyya, Rahul, and Shobit Omar. 2018. Influence of Excess Sodium Addition on the Structural Characteristics and Electrical Conductivity of  $\text{Na}_{0.5}\text{Bi}_{0.5}\text{TiO}_3$ . *Solid State Ionics* 317 (April): 115–21. <https://doi.org/10.1016/J.SSI.2018.01.016>.
8. Birol, Hansu, Dragan Damjanovic, and Nava Setter. 2005. Preparation and Characterization of  $\text{KNbO}_3$  Ceramics. *Journal of the American Ceramic Society* 88 (7): 1754–59. <https://doi.org/10.1111/j.1551-2916.2005.00347.x>.
9. Blum, Winfried E.H. 2013. Soil and Land Resources for Agricultural Production: General Trends and Future Scenarios-A Worldwide Perspective. *International Soil and Water Conservation Research* 1 (3): 1–14. [https://doi.org/10.1016/S2095-6339\(15\)30026-5](https://doi.org/10.1016/S2095-6339(15)30026-5).
10. Chen, Xiyong, Jie Zeng, Xia Yan, Mingxin Zhou, Peng Tang, Tianquan Liang, and Weizhou Li. 2017. Effects of Bi Deficiency on the Microstructural and Conductive Properties of  $\text{Na}_{0.5}\text{Bi}_{0.5}\text{TiO}_3$  (NBT) Perovskites. *Solid State Ionics* 309 (October): 152–62. <https://doi.org/10.1016/J.SSI.2017.07.024>.
11. Echatooui, NS, T Lamcharfi - ... & chemical news, and undefined 2005. n.d. Diffuse Phase Transition and Relaxation Behavior in Hydrothermally Processed PLZT Ceramics. *Physical and Chemical News*.
12. Elhorst, J. Paul. 2014. Matlab Software for Spatial Panels. *International Regional Science Review* 37 (3): 389–405. <https://doi.org/10.1177/0160017612452429>.
13. Eric Cross, L. 1987. Relaxor Ferroelectrics. *Ferroelectrics* 76 (1): 241–67. <https://doi.org/10.1080/00150198708016945>.
14. Fan, Gongduan, Zhong Chen, Zhongsen Yan, Banghao Du, Heliang Pang, Dingsheng Tang, Jing Luo, and Jiuyang Lin. 2021. Efficient Integration of Plasmonic Ag/AgCl with Perovskite-Type  $\text{LaFeO}_3$ : Enhanced Visible-Light Photocatalytic Activity for Removal of Harmful Algae. *Journal of Hazardous Materials* 409 (May): 125018. <https://doi.org/10.1016/J.JHAZMAT.2020.125018>.
15. Fouilleux, Eve, Nicolas Bricas, and Arlène Alpha. 2017. Feeding 9 Billion People: Global Food Security Debates and the Productionist Trap. *Journal of European Public Policy* 24 (11): 1658–77. <https://doi.org/10.1080/13501763.2017.1334084>.
16. González-Pleiter, Miguel, Soledad Gonzalo, Ismael Rodea-Palomares, Francisco Leganés, Roberto Rosal, Karina Boltes, Eduardo Marco, and Francisca Fernández-Piñas. 2013. Toxicity of Five Antibiotics and Their Mixtures towards Photosynthetic Aquatic Organisms: Implications for Environmental Risk Assessment. *Water Research* 47 (6): 2050–64. <https://doi.org/10.1016/J.WATRES.2013.01.020>.
17. Goutham, Cilaveni, Kinjarapu Venkata Ashok Kumar, Sai Santosh Kumar Raavi, Challapalli Subrahmanyam, and Saket Asthana. 2021. Enhanced Electrical and Photocatalytic Activities in  $\text{Na}_{0.5}\text{Bi}_{0.5}\text{TiO}_3$  through Structural Modulation by Using Anatase and Rutile Phases of  $\text{TiO}_2$ . *Journal of Materiomics*, no. xxxx. <https://doi.org/10.1016/j.jmat.2021.06.003>.
18. He, Rong'an, Shaowen Cao, Peng Zhou, and Jiaguo Yu. 2014. Recent Advances in Visible Light Bi-Based Photocatalysts. *Cuihua Xuebao/Chinese Journal of Catalysis*. Science Press. [https://doi.org/10.1016/s1872-2067\(14\)60075-9](https://doi.org/10.1016/s1872-2067(14)60075-9).
19. Herrmann, Jean-Marie. 1999. Heterogeneous Photocatalysis: Fundamentals and Applications to the Removal of Various Types of Aqueous Pollutants. *Catalysis Today*. Vol. 53.
20. Hiruma, Yuji, Hajime Nagata, and Tadashi Takenaka. 2006. Phase Transition Temperatures and Piezoelectric Properties of  $(\text{Bi}_{1/2}\text{Na}_{1/2})\text{TiO}_3$ - $(\text{Bi}_{1/2}\text{K}_{1/2})\text{TiO}_3$ - $\text{BaTiO}_3$  lead-Free Piezoelectric Ceramics. *Japanese Journal of Applied Physics, Part 1: Regular Papers and Short Notes and Review Papers* 45 (9 B): 7409–12. <https://doi.org/10.1143/JJAP.45.7409>.
21. Huo, Yuning, Zongli Xie, Xingdong Wang, Hexing Li, Manh Hoang, and Rachel A. Caruso. 2013. Methyl Orange Removal by Combined Visible-Light Photocatalysis and Membrane Distillation. *Dyes and Pigments* 98 (1): 106–12. <https://doi.org/10.1016/j.dyepig.2013.02.009>.
22. Jiang, Xiang Ping, Mei Lin, Na Tu, Chao Chen, and Yue Ming Li. 2010. Synthesis of  $\text{K}_{0.5}\text{Bi}_{0.5}\text{TiO}_3$  Nanowires and Ceramics by a Simple Hydrothermal Method. *Materials Science and Engineering B: Solid-State Materials for Advanced Technology* 175 (1): 90–93. <https://doi.org/10.1016/j.mseb.2010.06.010>.
23. Jiang, Yue, Wen-Fan Chen, Hongyang Ma, Hangjuan Ren, Sean Lim, Xinxin Lu, Ghazaleh Bahmanrokh, et al. 2021. Effect of Bi/Ti Ratio on  $(\text{Na}_{0.5}\text{Bi}_{0.5})\text{TiO}_3/\text{Bi}_4\text{Ti}_3\text{O}_{12}$  Heterojunction Formation and Photocatalytic Performance. *Journal of Environmental Chemical Engineering* 9 (6): 106532. <https://doi.org/10.1016/j.jece.2021.106532>.
24. Kreisel, J., A. M. Glazer, P. Bouvier, and G. Lucazeau. 2001. High-Pressure Raman Study of a Relaxor Ferroelectric: The  $\text{Na}_{0.5}\text{Bi}_{0.5}\text{TiO}_3$  Perovskite. *Physical Review B - Condensed Matter and Materials Physics* 63 (17): 1741061–610. <https://doi.org/10.1103/physrevb.63.174106>.
25. Kurra, Sreenu, Perala Venkataswamy, Gundeboina Ravi, Chandhiri Sudhakar Reddy, Boggu

- Jaganmohan Reddy, and Muga Vithal. 2019. Enhancement of Photocatalytic Activity of Sodium Bismuth Titanate by Doping with Copper, Silver, and Tin Ions. *Zeitschrift Fur Anorganische Und Allgemeine Chemie* 645 (5): 529–36. <https://doi.org/10.1002/zaac.201800337>.
26. Lahmar, A., K. Zhao, S. Habouti, M. Dietze, C. H. Solterbeck, and M. Es-Souni. 2011. Off-Stoichiometry Effects on BiFeO<sub>3</sub> Thin Films. *Solid State Ionics* 202 (1): 1–5. <https://doi.org/10.1016/J.SSI.2011.03.017>.
27. Lencka, Malgorzata M., Magdalena Oledzka, and Richard E. Riman. 2000. Hydrothermal Synthesis of Sodium and Potassium Bismuth Titanates. *Chemistry of Materials* 12 (5): 1323–30. <https://doi.org/10.1021/cm9906654>.
28. Li, Hui Dong, Chu De Feng, and Wen Long Yao. 2004. Some Effects of Different Additives on Dielectric and Piezoelectric Properties of (Bi<sub>1/2</sub>Na<sub>1/2</sub>)TiO<sub>3</sub>-BaTiO<sub>3</sub> Morphotropic-Phase-Boundary Composition. *Materials Letters* 58 (7–8): 1194–98. <https://doi.org/10.1016/J.MATLET.2003.08.034>.
29. Mesrar, M. 2022. DIELECTRIC MEASUREMENTS AND IMPEDANCE SPECTROSCOPY OF Ba-MODIFIED (Na<sub>0.5</sub>Bi<sub>0.5</sub>)TiO<sub>3</sub> PREPARED BY THE HYDROTHERMAL METHOD. *Ceramics - Silikaty* 66 (3): 0–0. <https://doi.org/10.13168/cs.2022.0039>.
30. Mesrar, M., A. Elbasset, N. S. Echatoui, F. Abdi, and T. Lamcharfi. 2023. Microstructural and High-Temperature Dielectric, Piezoelectric and Complex Impedance Spectroscopic Properties of K<sub>0.5</sub>Bi<sub>0.5</sub>TiO<sub>3</sub> Modified NBT-BT Lead-Free Ferroelectric Ceramics. *Heliyon* 9 (4): e14761. <https://doi.org/10.1016/j.heliyon.2023.e14761>.
31. Mesrar, M., T. Lamcharfi, N-S. Echatoui, and F. Abdi. 2022a. (1-x)(Na<sub>0.5</sub>Bi<sub>0.5</sub>)TiO<sub>3</sub>-x(K<sub>0.5</sub>Bi<sub>0.5</sub>)TiO<sub>3</sub> Ceramics near Morphotropic Phase Boundary: A Structural and Electrical Study. *Materialia*, March, 101404. <https://doi.org/10.1016/J.MTLA.2022.101404>.
32. Mesrar, M., T. Lamcharfi, N. Echatoui, F. Abdi, and A. Harrach. 2018. Investigation of Morphotropic Phase Boundary by Rietveld Refinement and Raman Spectroscopy for (1-x)(Na<sub>0.5</sub>Bi<sub>0.5</sub>)TiO<sub>3</sub>-xBaTiO<sub>3</sub> Ceramics. *Asian Journal of Chemistry* 30 (5): 1012–18. <https://doi.org/10.14233/ajchem.2018.21116>.
33. Mesrar, M., T. Lamcharfi, N. Echatoui, F. Abdi, A. Harrach, and F.Z. Ahjyaje. 2019. Hydrothermal Synthesis, Microstructure and Electrical Properties of (1-x)(Na<sub>0.5</sub>Bi<sub>0.5</sub>)TiO<sub>3</sub>-xBaTiO<sub>3</sub> Ceramics. *Moroccan Journal of Quantitative and Qualitative Research* 0 (1): 14–24.
34. Mesrar, M., T. Lamcharfi, N. S. Echatoui, and F. Abdi. 2022b. (1-x)(Na<sub>0.5</sub>Bi<sub>0.5</sub>)TiO<sub>3</sub>-x(K<sub>0.5</sub>Bi<sub>0.5</sub>)TiO<sub>3</sub> Ceramics near Morphotropic Phase Boundary: A Structural and Electrical Study. *Materialia* 22 (March). <https://doi.org/10.1016/j.mtla.2022.101404>.
35. Mesrar, Mohammed, Abdelhalim Elbasset, and F Abdi. 2023. Effect of Synthesis Process on the Piezoelectric Properties of (1-x) NBT-XBT : A Comparative Study between Solid State and hydrothermal. *International Journal of Nanoelectronics and Materials* Volume 16, No. 2, April 2023 [241-264]
36. Mesrar, Mohammed, Abdelhalim Elbasset, Nor Said Echatoui, Farid Abdi, and Taj Dine Lamcharfi. 2022. Studies of Structural, Dielectric, and Impedance Spectroscopy of KBT-Modified Sodium Bismuth Titanate Lead-Free Ceramics. *ACS Omega*. <https://doi.org/10.1021/acsomega.2c03139>.
37. Mesrar, Mohammed, Tajdine Lamcharfi, Nor-Said Echatoui, Farid Abdi, Fatima Zahra Ahjyaje, and Mustapha Haddad. 2019. Effect of Barium Doping on Electrical and Electromechanical Properties of (1-x)(Na<sub>0.5</sub>Bi<sub>0.5</sub>)TiO<sub>3</sub>-xBaTiO<sub>3</sub>. *Mediterranean Journal of Chemistry*. <https://doi.org/10.13171/10.13171/mjc8319050908mm>.
38. Moon, Kyoung Seok, Dibyanjan Rout, Ho Yong Lee, and Suk Joong L. Kang. 2011. Solid State Growth of Na<sub>1/2</sub>Bi<sub>1/2</sub>TiO<sub>3</sub> 3BaTiO<sub>3</sub> Single Crystals and Their Enhanced Piezoelectric Properties. *Journal of Crystal Growth* 317 (1): 28–31. <https://doi.org/10.1016/j.jcrysgro.2011.01.023>.
39. Mrabet, I. El, M. Kachabi, M. Nawdali, A. Harrach, F. Khalil, M. Ijjaali, M. Benzina, and H. Zaitan. 2018. Treatment of Landfill Leachate from Fez City (Morocco) Using Fenton and Photo-Fenton Processes. *IOP Conference Series: Earth and Environmental Science* 161 (1): 012025. <https://doi.org/10.1088/1755-1315/161/1/012025>.
40. Neusel, Claudia, and Gerold A. Schneider. 2014. Size-Dependence of the Dielectric Breakdown Strength from Nano- to Millimeter Scale. *Journal of the Mechanics and Physics of Solids* 63 (1): 201–13. <https://doi.org/10.1016/j.jmps.2013.09.009>.
41. Paola, Agatino Di, Elisa García-López, Giuseppe Marci, and Leonardo Palmisano. 2012. A Survey of Photocatalytic Materials for Environmental Remediation. *Journal of Hazardous Materials*. Elsevier. <https://doi.org/10.1016/j.jhazmat.2011.11.050>.
42. Pookmanee, Pusit, Gobwute Rujijanagul, Supon Ananta, Robert B. Heimann, and Sukon Phanichphant. 2004. Effect of Sintering Temperature on Microstructure of Hydrothermally Prepared Bismuth Sodium Titanate Ceramics. *Journal of the European Ceramic Society* 24 (2): 517–20. [https://doi.org/10.1016/S0955-2219\(03\)00197-3](https://doi.org/10.1016/S0955-2219(03)00197-3).
43. Quittet, A. M., M. I. Bell, M. Krauzman, and P. M. Raccach. 1976. Anomalous Scattering and Asymmetrical Line Shapes in Raman Spectra of Orthorhombic

- KNbO<sub>3</sub>. *Physical Review B* 14 (11): 5068–72. <https://doi.org/10.1103/PhysRevB.14.5068>.
44. Rietveld, H. M. 1967. Line Profiles of Neutron Powder-Diffraction Peaks for Structure Refinement. *Acta Crystallographica* 22 (1): 151–52. <https://doi.org/10.1107/s0365110x67000234>.
  45. Roukos, Roy, Sara Abou Dargham, Jimmy Romanos, Fatima Barakat, and Denis Chaumont. 2019. Complex Structural Contribution of the Morphotropic Phase Boundary in Na<sub>0.5</sub>Bi<sub>0.5</sub>TiO<sub>3</sub> - CaTiO<sub>3</sub> System. *Ceramics International* 45 (4): 4467–73. <https://doi.org/10.1016/j.ceramint.2018.11.126>.
  46. Shannon, Mark A., Paul W. Bohn, Menachem Elimelech, John G. Georgiadis, Benito J. Mariñas, and Anne M. Mayes. 2008. Science and Technology for Water Purification in the Coming Decades. *Nature* 452 (7185): 301–10.
  47. Shih, Duke P.C., Ainara Aguadero, and Stephen J. Skinner. 2018. Improvement of Ionic Conductivity in A-Site Lithium Doped Sodium Bismuth Titanate. *Solid State Ionics* 317 (April): 32–38. <https://doi.org/10.1016/J.SSI.2018.01.003>.
  48. Sidi, Mohammed Mesrar, Mohamed Ben, F Abdi Sidi, Mohammed Mesrar, Tajdine Lamcharfi, Nor-Said Echadou, Farid Abdi, and Ahmed Harrach. 2019. High Dielectric Constant of (1-x)(Na<sub>0.5</sub>Bi<sub>0.5</sub>)TiO<sub>3</sub>-xBaTiO<sub>3</sub> Prepared by the Hydrothermal Method. Article in *Mediterranean Journal of Chemistry*. 2019.
  49. Suchanicz, J., and J. Kwapuliski. 1995. X-Ray Diffraction Study of the Phase Transitions in Na<sub>0.5</sub>Bi<sub>0.5</sub>TiO<sub>3</sub>. *Ferroelectrics* 165 (1): 249–53. <https://doi.org/10.1080/00150199508228304>.
  50. Suchanicz, Jan, Irena Jankowska-Sumara, and Tatiana V. Kruzina. 2011. Raman and Infrared Spectroscopy of Na<sub>0.5</sub>Bi<sub>0.5</sub>TiO<sub>3</sub> - BaTiO<sub>3</sub> Ceramics. *Journal of Electroceramics* 27 (2): 45–50. <https://doi.org/10.1007/s10832-011-9648-5>.
  51. Sui, H. T., D. M. Yang, H. Jiang, Y. L. Ding, and C. H. Yang. 2013. Preparation and Electrical Properties of Sm-Doped Bi<sub>2</sub>Ti<sub>2</sub>O<sub>7</sub> Thin Films Prepared on Pt (111) Substrates. *Ceramics International* 39 (2): 1125–28. <https://doi.org/10.1016/j.ceramint.2012.07.035>.
  52. Sundarakannan, B., K. Kakimoto, and H. Ohsato. 2003. Frequency and Temperature Dependent Dielectric and Conductivity Behavior of KNbO<sub>3</sub> Ceramics. *Journal of Applied Physics* 94 (8): 5182–87. <https://doi.org/10.1063/1.1610260>.
  53. Swain, Sridevi, Subrat Kumar Kar, and Pawan Kumar. 2015. Dielectric, Optical, Piezoelectric and Ferroelectric Studies of NBT–BT Ceramics near MPB. *Ceramics International* 41 (9): 10710–17. <https://doi.org/10.1016/j.ceramint.2015.05.005>.
  54. Tang, Junwang, Zhigang Zou, and Jinhua Ye. 2005. Kinetics of MB Degradation and Effect of PH on the Photocatalytic Activity of MIn<sub>2</sub>O<sub>4</sub> (M = Ca, Sr, Ba) under Visible Light Irradiation. *Res. Chem. Intermed* 31 (6): 513–19.
  55. Tanji, Karim, J. A. Navio, Jamal Naja, M. C. Hidalgo, Abdellah Chaqroune, C. Jaramillo-Páez, and Abdelhak Kherbeche. 2019. Extraordinary Visible Photocatalytic Activity of a Co<sub>0.2</sub>Zn<sub>0.8</sub>O System Studied in the Remazol BB Oxidation. *Journal of Photochemistry and Photobiology A: Chemistry* 382 (May): 111877. <https://doi.org/10.1016/j.jphotochem.2019.111877>.
  56. Tanji, Karim, Morad Zouheir, Yassine Naciri, Hassan Ahmoum, Abdelghani Hsini, and Oumaima Mertah. 2022. Visible Light Photodegradation of Blue Basic 41 Using Cobalt Doped ZnO : Box-Behnken Optimization and DFT Calculation. *Journal of the Iranian Chemical Society* 19: 2779–2794. <https://doi.org/10.1007/s13738-022-02496-w>.
  57. Trelcat, Jean François, Sophie d’Astorg, Christian Courtois, Philippe Champagne, Mohamed Rguiti, and Anne Leriche. 2011. Influence of Hydrothermal Synthesis Conditions on BNT-Based Piezoceramics. *Journal of the European Ceramic Society* 11 (31): 1997–2004. <https://doi.org/10.1016/J.JEURCERAMSOC.2011.04.025>.
  58. Xiao, Qi, Jiang Zhang, Chong Xiao, and Xiaoke Tan. 2007. Photocatalytic Decolorization of Methylene Blue over Zn<sub>1-x</sub>CoxO under Visible Light Irradiation. *Materials Science and Engineering B: Solid-State Materials for Advanced Technology* 142 (2–3): 121–25. <https://doi.org/10.1016/j.mseb.2007.06.021>.
  59. Yang, Zetian, Feng Gao, Hongliang Du, Li Jin, Leilei Yan, Qingyuan Hu, Ying Yu, et al. 2019. Grain Size Engineered Lead-Free Ceramics with Both Large Energy Storage Density and Ultrahigh Mechanical Properties. *Nano Energy* 58 (April): 768–77. <https://doi.org/10.1016/j.nanoen.2019.02.003>.
  60. Yang, Zhengwen, Ji Zhou, Xueguang Huang, Qin Xie, Ming Fu, Bo Li, and Longtu Li. 2009. Preparation and Photonic Bandgap Properties of Na<sub>1/2</sub>Bi<sub>1/2</sub>TiO<sub>3</sub> Inverse Opal Photonic Crystals. *Journal of Alloys and Compounds* 471 (1–2): 241–43. <https://doi.org/10.1016/j.jallcom.2008.03.068>.
  61. Zeroual, S., H. Lidjici, W. Chatta, and H. Khe-makhem. 2019. Dielectric and Raman Spectroscopy Studies of (Na<sub>0.5</sub>Bi<sub>0.5</sub>)TiO<sub>3</sub> Lead-Free Ceramic. *Ceramica* 65 (374): 222–26. <https://doi.org/10.1590/0366-69132019653742627>.